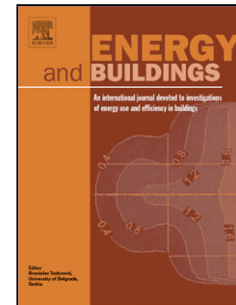


## Accepted Manuscript

Title: Development of a fine-scale discomfort index map and its application in measuring living environments using remotely-sensed thermal infrared imagery

Authors: Hanqiu Xu, Xiujuan Hu, Huade Guan



PII: S0378-7788(17)30794-6  
DOI: <http://dx.doi.org/doi:10.1016/j.enbuild.2017.06.003>  
Reference: ENB 7666

To appear in: *ENB*

Received date: 7-3-2017  
Revised date: 3-5-2017  
Accepted date: 6-6-2017

Please cite this article as: Hanqiu Xu, Xiujuan Hu, Huade Guan, Development of a fine-scale discomfort index map and its application in measuring living environments using remotely-sensed thermal infrared imagery, Energy and Buildings <http://dx.doi.org/10.1016/j.enbuild.2017.06.003>

This is a PDF file of an unedited manuscript that has been accepted for publication. As a service to our customers we are providing this early version of the manuscript. The manuscript will undergo copyediting, typesetting, and review of the resulting proof before it is published in its final form. Please note that during the production process errors may be discovered which could affect the content, and all legal disclaimers that apply to the journal pertain.

# Development of a fine-scale discomfort index map and its application in measuring living environments using remotely-sensed thermal infrared imagery

Hanqiu Xu <sup>a,b,c,\*</sup>, Xiujuan Hu <sup>a,b,d</sup>, Huade Guan <sup>e</sup>

*a. College of Environment and Resources, Fuzhou University, Fuzhou 350116, China; b. Fujian Key Laboratory of Remote Sensing of Soil Erosion, Fuzhou 350116, China; c. Key Laboratory of Spatial Data Mining & Information Sharing of Ministry of Education, Fuzhou University, Fuzhou 350116, China; d. Institute of Remote Sensing Information Engineering, Fuzhou 350116, China; e. School of the Environment, Flinders University, Adelaide, SA 5001, Australia*

Corresponding author: Hanqiu Xu

College of Environment and Resources, Fuzhou University, Fuzhou 350116, China

Email: [hxu@fzu.edu.cn](mailto:hxu@fzu.edu.cn)

Tel: +86-591-22866071

## Highlights

- Deriving discomfort index using a sharpened 10 m resolution satellite thermal infrared image
- Representing thermal discomfort levels of a city with a fine-scale DI map rather than a single value
- Revealing spatial differences of human thermal discomfort sensation in a city
- Determining the characteristics of living environments corresponding to different DI grades
- Discovering the differences in the contributions of built land, vegetation and water to DI

**Abstract:** The discomfort index (DI) is an important indicator that measures human heat sensation for different climate conditions. Currently, DI of a city is usually calculated using the data from a single or a few weather stations and hence does not accurately represent various thermal discomfort states of the whole city. In addition, because the result of existing DI is just a single numeric value, it does not reveal the spatial differences of thermal discomfort levels and thus is unable to be related to actual living environment conditions. This greatly limits the DI application. Taking Fuzhou of southeastern China as an example, this paper proposes a technique to produce a fine-scale DI map by combining remotely-sensed thermal infrared data with in-situ measured meteorological data. The DI map clearly reveals the spatial details of the DI in different locations of the city. It provides quantitative characterization of the living environment of each DI level based on a 3-graded DI map. This greatly expands the application range of the index. Quantitative analysis results show that the area of high building density substantially increases human thermal discomfort sensation, while high vegetation and water covers reduce the sensation. The impact of buildings to human discomfort sensation is near two times more than those of the vegetation and water in the Fuzhou case.

**Key words:** thermal comfort; discomfort index; living environment; remote sensing; Fuzhou

## 1. Introduction

Global warming and climate change has brought serious challenges to human living environments dominated by buildings [1,2]. Rapid urbanization-induced urban heat islands (UHI) can further deteriorate outdoor human thermal comfort in warm season. In general, thermal comfort occurs at air temperatures between 18 and 23°C and relative humidity between 35 and 70% [3]. Satisfaction with the thermal environment to which a person is exposed influences his/her health and work productivity. Workers who are satisfied with their thermal environment are more productive [4,5]. On the other hand, thermal discomfort can lead to the sick building syndrome [6].

There are currently a number of indicators developed to assess human thermal response to ambient conditions [7] and to support the design of buildings [8]. Of them, the discomfort index (DI) of Thom [9] is a measure of the degree of discomfort experienced by an individual in warm weather. The index is a combination of temperature and humidity that evaluates how current temperature and relative humidity affect the discomfort sensation and cause health risk in the population. The DI has been commonly included as a routine variable in public meteorological forecasts, as well as many related studies [10-13].

Assessing thermal comfort in extreme hot summer season is a major application field of the Thom's DI. Studies on thermal comfort conditions on the islands of the Mediterranean Sea using the DI have noticed that

the highest DI occurred in August based on the records of meteorological stations [10]. Mean daily and hourly variations of the DI in hot summer of Athens were used to predict consecutive hours characterized by high DI values [14]. Silva et al. [15] investigated the UHI and the thermal discomfort level in the city of Campina Grande, Brazil, and found that the city in summer had partially comfortable conditions, while in winter was fully comfortable. The hourly DI values changed significantly between the two seasons. Analysis of the thermal comfort of various building environments in Malaysia has led to development of a new DI range for tropical climate countries by a correlation of human thermal sensation with Thom's DI [11].

The DI has also been applied to study its relationship with other environmental factors. Studies investigating the effects of green spaces to urban thermal environment suggest that evapotranspiration of plants decreases DI values because evaporation of water increased the relative humidity and reduces temperature [16]. Giannaros and Melas [12] investigated the UHI in Thessaloniki of Greece and found the UHI had a negative impact on thermal comfort. They showed that a 1.5 °C increase in the UHI intensity would result in an average 1°C increase in DI. Recently, a synergetic effect between air pollution and discomfort conditions was found during extreme hot weather days in three Greek cities, which revealed that the comfort conditions in the city center became more unfavorable during hot days than the days of average conditions [17].

A few studies have employed satellite remote sensing techniques to estimate Thom's DI values for the past decade. The thermal infrared data of the Advanced Very High Resolution Radiometer (AVHRR) sensor on board the National Oceanic and Atmospheric Administration (NOAA) satellite have been used to estimate DI [3]. The work has achieved a good agreement ( $R^2 = 0.79$ ) between resultant satellite-derived DI and the coincident DI calculated from the data recorded at weather stations, showing the potential of using satellite data for defining the spatial variation of the DI values at 1.1 km resolution. Recently, Polydoros and Cartalis [18] used the method of [3] to produce a DI map using the thermal infrared images of AVHRR and related the DI values with built-up land features. They found that the DI values were correlated to built-up land features during heat wave events.

Although the Thom's DI has been frequently applied in various fields, its application has suffered three main problems:

(1) The DI of a city is usually calculated based on the meteorological data from one or a few weather stations. Heterogeneity of the urban environment, however, makes single point surface measurements less representative of the city [19]. Therefore, such a weather station-measured DI is incapable of capturing the

thermal discomfort conditions of the whole city due to the limited number of weather stations. In addition, the existing DI lacks visibility because it usually uses a single numerical value to represent the thermal performance of various building-dominated living environments of a city.

(2) The DI is used in the meteorological field mainly for a forecast of thermal conditions. Its significance in ecological environment aspect has not been fully mined. The quantitative relationship between human sensation of thermal comfort and its corresponding ecological environment quality has not been fully explored.

(3) There are quite a few DI applications using remote sensing techniques. A literature search from Web of Science<sup>TM</sup> only finds two related papers mentioned above. They both used AVHRR thermal infrared imagery to derive Thom's DI values. Remote sensing greatly improves the spatial detail of DI, when compared with that of the traditional DI calculated from sparsely-spaced weather stations. However, the coarse resolution of the image makes the illustration of the spatial variations in the resultant DI map be limited to the resolution of the AVHRR pixel at 1.1 km.

In order to solve the above-mentioned problems and to further explore the potential application of DI, this paper proposes a technique to produce a fine-scale DI map at 10 m resolution using remote sensing techniques. The produced DI map can reveal spatial details of the DI values over a large area. In addition, the fine-scale DI estimates will permit urban and building designers to relate the DIs to various built environments so that the characteristics of the living conditions corresponding to different DI levels can be identified. This adds new value to the traditional DI applications. A clear understanding of spatial details about thermal comfort conditions is essential for urban and building designers.

## **2. Methodology**

### **2.1. Study area and data**

Fuzhou is the capital of Fujian province in southeastern China (118°08'–120°31'E, 25°15'–26°39'N). The city is located in an estuary basin surrounded by mountainous terrain with elevations ranging from 600 to 1000 m above sea level (Fig. 1a). As a result, it has poor natural ventilation. Fuzhou has a subtropical monsoon climate with average annual temperature of 23 °C and a mean annual precipitation of 900–2100 mm.

During the last three decades, Fuzhou city has witnessed a fast urban expansion. This has caused a remarkable change in the city's thermal environment and development of severe UHI in the city [20]. Data from China Meteorological Data Network (<http://data.cma.cn>) show that the average annual number of hot days (air temperature > 35 °C) during 1981–2010 is 33, ranking at the top of the provincial capital cities in China. Fuzhou is hence dubbed by media as “Top of China's three new furnace cities” and “China's hottest

provincial capital city". Therefore, the Fuzhou basin area is selected for this study, which covers an area of 583 km<sup>2</sup> (Fig. 1b).

Satellite remotely-sensed thermal infrared data have long been an important data source for monitoring dynamics of the land surface temperature (LST). Of them, the thermal infrared band of Landsat series images is most commonly used. The LST can be obtained by inversion of thermal infrared information of the band. According to the availability and quality of images, two satellite images were chosen for this study: a Landsat 8 image (Level 1T) acquired on June 25, 2016 at 10: 33, and a Sentinel 2A image (Level 1C) of June 23, 2016 at 10: 50. The two images were downloaded from the Landsat website of the U.S. Geological Survey and (USGS) and the Sentinel 2 website of the European Space Agency (ESA), respectively.

Fuzhou city has only two state-run weather stations. Therefore, the meteorological data used in this study were mainly collected from these two stations: Wushan National Datum Weather Station (Wushan) and Jin'an Weather Station (Jin'an). In addition, the data from the weather station on new campus of Fuzhou University (FZU) run by the university were also used. Furthermore, we measured meteorological data on June 24, 2016 between 10:30 and 10:50, the duration of the two satellite overpass. Although there are date differences between two images and in situ-measured data, there was no significant change of the weather conditions among these days (Table 1).

## 2.2. Discomfort Index

The Thom's DI has been widely used in the world for evaluating human discomfort degree in summer. It estimates human thermal sensation by the combination of temperature and humidity [9]. Epstein and Moran [4] suggested using DI as a universal heat stress index. The result of Pantavou et al. [21] indicated a good relationship of the DI with severe heat stress conditions.

Initially, the DI was introduced as a function of dry-bulb and wet-bulb temperatures expressed as:

$$DI = [(T_d + T_w)/2] + 0.1[-150 - (T_d + T_w)] \quad (1)$$

where  $T_d$  is the dry bulb temperature in °F, and  $T_w$  is the wet bulb temperature in °F.

Later it was modified using air temperature and relative humidity [22]:

$$DI = T_a - 0.55 (1 - 0.01 RH) (T_a - 14.5) \quad (2)$$

where  $T_a$  is the air temperature in °C, and  $RH$  is the relative humidity in %. The index is essentially an effective temperature based on air temperature and humidity.

The results of DI computation are in good agreement with effective temperature for a range of ambient temperatures and related humidity. It is usually divided into six grades. Grades from 1 ( $DI < 21$  °C) to 6 ( $DI \geq 32$  °C) represent the degrees from comfort to extremely uncomfortable [18].

### 2.3. Retrieval and sharpening of LST

According to Eq. 2, DI is calculated using air temperature and relative humidity. However, both of them can not be estimated directly from remote sensing data because there is no effective and reliable algorithm that directly converts remote sensing data to either air temperature or relative humidity. A common method currently used is to convert remotely-sensed thermal infrared information into LST first, and then transform the LST into air temperature as LST is correlated with air temperature. Satellite-generated LST is the radiating temperature of the land surface retrieved from thermal infrared channels of satellite sensors [19].

The used Landsat 8 thermal infrared sensor (TIRS) has two thermal infrared bands, TIRS bands 10 and 11. Due to the problems occurring in the calibration of TIRS band 11, as announced by the Landsat 8 project team [23,24], this study utilized band 10 to retrieve LST. The method used to do the retrieval is the single channel algorithm of Jiménez-Muñoz et al. [25], expressed as:

$$LST = \gamma [\varepsilon^{-1}(\psi_1 L + \psi_2) + \psi_3] + \delta \quad (3)$$

$$L = M_L Q_{cal} + A_L \quad (4)$$

$$\gamma \approx T^2 / (b_\gamma L), \quad \delta \approx T - T^2 / b_\gamma \quad (5)$$

$$T = K2 / \ln(K1/L + 1) \quad (6)$$

where  $L$  is the at-sensor radiance of TIRS band 10 in  $W/(m^2 \cdot sr \cdot \mu m)$ ,  $M_L$  and  $A_L$  are the gain and bias of the band, respectively, in  $W/(m^2 \cdot sr \cdot \mu m)$ ,  $Q_{cal}$  is the digital number of band 10,  $T$  is the brightness temperature of the band in Kelvin, and  $K1$  and  $K2$  are the calibration constants of band 10.  $M_L$ ,  $A_L$ ,  $K1$  and  $K2$  can be obtained from the head file of the image.  $b_\gamma = 1324$  K,  $\varepsilon$  is the land surface emissivity (unitless), estimated from the ASTER spectral library and the result of Nichol [26]. The emissivity of forest, grass, soil, built-up land and water for band 10 is 0.9813, 0.9823, 0.9722, 0.9212 and 0.9908, respectively.  $\psi_1$ ,  $\psi_2$ ,  $\psi_3$  are the atmospheric functions that can be calculated using following equations:

$$\psi_1 = 1/\tau, \quad \psi_2 = -L^\downarrow - L^\uparrow/\tau, \quad \psi_3 = L^\downarrow \quad (7)$$

where  $\tau$  is the atmospheric transmission (unitless),  $L^\uparrow$  is the upwelling atmospheric radiance (path radiance) in  $W/(m^2 \cdot sr \cdot \mu m)$ , and  $L^\downarrow$  is the downwelling atmospheric radiance (sky radiance) in  $W/(m^2 \cdot sr \cdot \mu m)$ . For TIRS band 10,  $\tau$ ,  $L^\uparrow$  and  $L^\downarrow$  are 0.48, 4.45  $W/(m^2 \cdot sr \cdot \mu m)$  and 6.55  $W/(m^2 \cdot sr \cdot \mu m)$ , respectively, obtained from the Atmospheric Correction Parameter Calculator of Barsi et al. [27] based on the Fuzhou's geographical location and the date and time of the Landsat 8 satellite overpass.

Despite being finer than 1000 m resolution of AVHRR, the 100 m resolution of TIRS band 10 image is still too coarse to resolve the thermal effects of many features (e.g., streets and building blocks) in urban environment. Higher spatial resolution for urban climatology study is always expected as finer pixel size can

have a closer correspondence to urban features [28]. Therefore, the retrieved LST image was further sharpened using the TsHARP algorithm of Agam et al. [29].

The TsHARP incorporates visible and near-infrared wavebands of a higher spatial resolution sensor to enhance a single thermal band. The assumption of the TsHARP is that a unique relationship between radiometric surface temperature and vegetation index exists across spatial resolutions. Therefore, the coarser resolution thermal infrared image can be sharpened through the assistance of the vegetation index computed using high resolution visible and near-infrared wavebands. In this case, the retrieved 100 m resolution LST image was sharpened to 10 m resolution with the near synchronous, 10 m resolution Sentinel 2A image. A single pixel of the Landsat 8 TIRS image at 100 m resolution corresponds to pixel blocks composed of 100 pixels of the visible and near-infrared bands of Sentinel 2A image at 10 m resolution. Therefore, the 100 m pixel of Landsat 8 TIRS image can be downscaled to 10 m resolution with the normalized difference vegetation index (NDVI) of Rouse et al. [30] derived using the red and near-infrared bands of the 10 m Sentinel 2A image. More details about the TsHARP method can be found in Agam et al. [29].

#### **2.4. Retrieval of air temperature**

Air temperature data are typically acquired from measurements recorded in weather stations. Due to the limitation in the number of weather stations, these in situ-measured air temperature data can offer only limited information about spatial details of the temperature over a wide area [6]. Therefore, as mentioned previously, the spatial distribution of air temperature on a regional scale is usually obtained from remote sensing thermal images based on the correlation of their LST products with in situ-measured air temperatures. The MODIS- and AVHRR-derived LSTs are commonly used for retrieving air temperature [3] [5,6] [18,19] [31,32]. However, over 1000 m resolution of the LST of either MODIS or AVHRR makes it spatially insufficient to distinguish the details of urban thermal environments and causes a relative low accuracy with errors generally fall in a range of 2–3 °C, exceeding the range of precision generally considered as 1–2 °C [6]. To overcome this problem, this study employed a sharpened 10 m-resolution LST image, aiming to detail more spatial differences of air temperature in urban thermal environments and to achieve a higher accuracy of retrieved air temperature.

Air temperature and relative humidity were measured using Testo 635-2 at 1.5 meter above the surface for main land cover types of Fuzhou in three different locations near the three weather stations. This equipment can be operated in a temperature range from -40 °C to 150 °C with accuracy of  $\pm 0.2$  °C, and also for measuring relative humidity, ranging from 0 to 100% with accuracy of  $\pm 3.0\%$ . The measurement was carried



out on June 24, 2016 between 10:30 and 10:50, the interval when Landsat 8 and Sentinel 2A overpass. A total of 176 surface objects were measured for air temperature and relative humidity. Table 2 lists the average air temperature and relative humidity of each measured objects.

Regression analysis for estimating air temperature was carried out using the measured air temperature and the sharpened 10 m-resolution LST image. This yielded a regression equation and a resultant coefficient of determination ( $R^2$ ) of 0.8816:

$$T_a = -0.0012 LST^2 + 0.1811 LST + 31.016 \quad (R^2 = 0.8816) \quad (8)$$

where  $T_a$  is air temperature in °C.

The model is statistically significant, with a  $p$ -value much less than 0.01 (one-tailed: 0.0014, two-tailed: 0.0029). Fig. 2 shows that the air temperature is correlated with the LST via a polynomial function. The high value of  $R^2$  suggests a strong agreement between  $LST$  and  $T_a$ , as the value is often used to describe how well a regression line fits a set of data. This implies that air temperature at the time of satellite overpass can be simulated with the Landsat 8 retrieved LST using the above regression equation.

## 2.5. Retrieval of relative humidity

Following the same approach for retrieving air temperature, the in situ-collected relative humidity was correlated to the sharpened Landsat 8 LST. The regression analysis shows that a polynomial model also achieves a higher degree of agreement than a linear model (Fig. 3). The polynomial model is expressed as:

$$RH = -0.0008LST^3 + 0.1093LST^2 - 5.0429LST + 125.63 \quad (R^2 = 0.823) \quad (9)$$

where  $RH$  is the relative humidity in %.

The regression is significant with low  $p$  values (one-tailed: 0.0018, two-tailed: 0.0036). An  $R^2$  of 0.823 suggests that the Landsat 8 retrieved  $LST$  agrees well with the in situ-measured  $RH$ , and thus can be used to estimate the relative humidity.

## 3. Results

The air temperature and relative humidity of the study area were retrieved with the sharpened 10 m LST using two regression-derived Eqs (8) and (9), respectively. This yielded a root mean square error (RMSE) of 0.82 °C between the in situ-measured and estimated air temperatures, and a RMSE of 2.05% between in situ-measured and estimated relative humidity. The estimated air temperature and relative humidity data were then used as independent variables to compute the DI values using Eq. (2). This finally produced the DI image for the Fuzhou basin for the satellite overpass time.

### 3.1. Validation

The validation of the satellite-estimated DI, along with air temperature and relative humidity, was carried

out at the locations of the three weather stations. The satellite-estimated data of June 25, 2016 were compared with the corresponding in situ measured data of the same day recorded in the three weather stations – Wushan, Jin'an and FZU. Each DI of the three weather stations was calculated using its own in situ-measured air temperature and relative humidity data based on Eq. (2). Because the data provided by weather stations are hourly data, they have to be interpolated to obtain the synchronous data at the time of the Landsat 8 satellite overpass (10:33 am local time) before they can be compared.

The comparison results show that the percent differences between weather station and satellite-derived data are all less than 5% (Table 3). As for the DI, the maximum error is less than 1°C or 3.3%. Regarding to the air temperature, the minimum and maximum differences achieved were 0.50 °C and 1.19 °C, respectively. The comparison indicates that the satellite based estimation performs well and the estimated results are reliable.

### 3.2. Classification of the DI image

Fig. 4a is the satellite-estimated DI image of the Fuzhou basin. The image shows that DI in the whole basin has clear spatial variability. The deeper the red color in the image, the lower the thermal comfort level of the representing area. Spatially, the thermal comfort level at the centre of the basin is obviously lower than surrounding suburbs, while the thermal comfort level in eastern basin is inferior to that in west. The visible DI image makes it more meaningful in its application as the thermal comfort level of the whole basin is now represented by a number of DI values rather than just a single DI value used in traditional method. Consequently, the DI level can be spatially distinguished in detail.

Further statistics for the DI image shows that the DI of the Fuzhou basin has a dynamic range from 27.09 to 33.16 °C, with a mean of 30.6 °C and a standard deviation of 1.16 °C. This indicates that the DI of the basin can be divided into three grades corresponding to Grades 4 to 6 of Thom's classification schema (Table 4, Fig. 4b). Among the three grades, the area of Grade 5 accounted for 66% of the basin area, suggesting that everyone in the basin feels severe heat stress, followed by Grade 4 (26.6%) and then Grade 6 (7.5%). The latter represents a few extremely hot regions.

### 3.3. Characteristics of living environments of three DI grades

The DI describes the relationship between a certain living environment and human thermal perception [7]. Unfortunately, the characteristics of the living environment corresponding to a certain DI level have rarely been investigated. In the Fuzhou case, the satellite-revealed three DI grades indicate that even in a general hot

weather condition, human feeling for thermal discomfort is still different spatially. Obviously, this is related to the local living environment (buildings and other enclosures) corresponding to each DI level and thus is another important issue concerned in this paper.

Built land, vegetation and water body are the three main land cover types of living environments and thus are three major factors that have the closest relation with the human living environment. For example, alterations in the amount of building and vegetation covers can influence the thermal properties of the ground surface by the amount of water vapor released into the air through evapotranspiration [19]. Obviously, the interaction of the three factors can have a significant influence on human thermal perception for a living environment. Therefore, the relationship of the DI with built land, vegetation and water body needs to be investigated.

Three commonly-used remote sensing indices, the Index-based Built-up Index (IBI) of Xu [33], the Normalized Difference Vegetation Index (NDVI) of Rouse et al. [30] and the Modified Normalized Difference Water Index (MNDWI) of Xu [34], were employed to extract the information of built land, vegetation and water body from the study area, respectively. The area of each land cover type was also calculated from its extracted thematic information (Table 4). Because the three indices have been successfully used in various applications [18] [35-38], the details of the three indices are not provided here.

The characteristics of the living environment corresponding to the DI grades were differentiated with the three land cover types (Table 4). In Grade 4, which represents a relative low DI environment in this case ( $27^{\circ}\text{C} \leq \text{DI} < 29^{\circ}\text{C}$ ), the vegetation and water areas account for about 50% each, whereas built cover only occupies 1% (Fig. 5a), suggesting a vegetation- and open water-dominated environment. Nevertheless, because the temperature of the study day (June 25, 2016) was quite high ( $33\text{--}34^{\circ}\text{C}$  at three weather stations), the majority of people might still feel uncomfortable even in such a living environment. In Grade 5 ( $29^{\circ}\text{C} \leq \text{DI} < 32^{\circ}\text{C}$ ), the percentage of building cover rises sharply to 55%, followed by a dramatically fall of water cover to less than 4%, as well as a drop of vegetation by 12 percentage points, indicating a living environment with many buildings, fewer trees/grasses and very few waters. In such a living environment, everyone feels hot and discomfort (Fig. 5b). In the living environment of Grade 6 ( $\text{DI} \geq 32^{\circ}\text{C}$ ), built surface accounts for more than 95%, while vegetation-covered area is less than 5%. There is almost no water. In such a living environment, human health will be seriously affected (Fig. 5c). This very high-density building area is lack of vegetation and water coverage and thus in favor of sensible heat exchange, which would intensify the thermal discomfort level.

### 3.4. Contribution of the three major land cover types to DI

Although built, vegetation and water covers are all factors affecting DI, the magnitudes of their contributions to DI may be different. Therefore, we need to know how much the individual factors are correlated with DI. We measured that through regression analysis. To perform this analysis, the IBI, NDVI and MNDWI were normalized within [0, 1] as recommended by Goetz et al. [39]. This permits analysis of each index as a continuous variable from 0 to 1 and allows the use of the indices as a percentage indicator when multiplied by 100. The normalized three index images were then combined with the DI image to form a four layer image (Fig. 6a).

The 4-layer image was randomly sampled across the whole image using a grid sampling method. A total of 16255 pixels were sampled, which were used for regression analysis to investigate the impact of the three factors on DI. The across-image sampling with large sampling numbers avoids the shortcoming of simple random sampling regarding the coverage of a whole image with insufficient samples [40,41] and would examine the relationship of the DI with the three factors in a more objective and detailed way.

The multivariate regression yielded the following function (significant at 0.03 levels):

$$DI = 5.688Building - 1.236Veg - 0.784Water + 28.19 \quad (R^2 = 0.91) \quad (10)$$

The model reveals that the vegetation and water are inversely correlated with DI, while the built land has a positive relationship with DI. This indicates that in summer vegetation and water help reduce thermal discomfort, while built land works inversely.

A 3-D spectral feature space plot was constructed using the DI and two factors – building and vegetation that have the largest and second largest impact on DI (to be analyzed below). The 16255 sampled pixel points are scattered in a cuneiform shape within the spectral feature space, big in head and sharp in bottom (Fig. 6b). From the 3 D scatter plot, it can be found that the pixels representing relative low DI values (Grade 4), together with the pixels with high vegetation and low building values, occur in the lower part of the scatter wedge. Such living environments in the Fuzhou basin make up only 26.63% of the area (Table 4), so the bottom of the wedge body has a tapering shape. While the upper part of the scatter wedge is composed of the pixels depicting high DI, high building but low vegetation cover areas, which account for most of the basin area and thus constitute a thick wedge head.

To quantitatively examine the magnitudes of the contributions of built land, vegetation and water to the DI, we measured the regression coefficients of the three independent variables in Eq. (10). According to the equation, the built land has a coefficient of 5.688, which is much greater than the sum of the coefficients of

vegetation and water (1.236+0.784). This indicates that the building has the greatest influence on DI, and is the most important factor that affects human thermal sensation. Accordingly, to reduce human thermal discomfort, the most efficient way is to avoid high density of buildings.

A quantitative analysis was further conducted to evaluate the interaction of three land cover types on the DI levels. Based on the strong fit of Eq. (10) and the normalized values of the IBI, NDVI and MNDWI mentioned previously, each 0.1 (10%) decrement of built cover with the increment in vegetation and water by 0.05 (5%) each would lower the DI value by 0.67 °C, or with the increment in vegetation or water by 0.1 (10%) would decrease the DI value by 0.69 °C or 0.65 °C, respectively. The analysis suggests that in the high-density built cover area, the decrease in built cover with the increase in vegetation and water cover can significantly mitigate thermal discomfort level because the greater water and vegetation cover suggests comparatively higher rates of evapotranspiration and favoring of latent over sensible heat exchange between surface and the atmosphere [42]. The revealed quantitative relationship between three land cover types is helpful for urban and building designers to predict thermal comfort effect of their plan works.

#### 4. Discussion

Maintaining thermal comfort for living environment is one of the important goals of urban planning and building designing. Therefore, the thermal environment should be evaluated more effectively. To date, DI has played an important role in evaluating the thermal comfort conditions [11,18]. The fine-scale DI map developed in this study makes the DI more meaningful and useful in investigating thermal comfort level of living environments for a large area.

With the visible DI map, the thermal environment becomes more understandable as it displays spatial variations and details of the DI values. On the other hand, irregularly and sparsely spaced weather stations make DI less insightful into the regional thermal environment. A satellite-derived DI map at the resolution of remote sensing imagery can provide information to regions void of the DI measurements between weather stations [19].

A leveled DI map further reveals the advantage of satellite-estimated DI over the traditional weather station-derived DI. According to data in Table 3, the DI values of three weather stations range from 29.2 to 29.67 °C, which all correspond to Grade 5, suggesting that the Fuzhou basin is only at one level of DI conditions on that day when predicted with the weather station-derived DI. In contrast, the satellite-estimated DI reveals three DI levels for the basin. About 35% of the basin area is not in Grade 5 discomfort condition, but in either Grade 4 or Grade 6 condition (Table 4). Therefore, the traditional weather station-produced DI is

unable to objectively represent the thermal discomfort condition of the whole Fuzhou basin. The subdivision of the satellite-derived DI allows a full understanding of the characteristics of the living environment corresponding to each DI grade. This can be useful for improving living conditions and reducing thermal discomfort sensation.

Even if the basin area is predicted only in a single numeric value, the satellite-derived DI is still more accurate than the weather station-derived one. According to Table 3, the average DI of the three weather stations is 29.4 °C, while the figure of the satellite method, taken from the mean of the DI image, is 30.6 °C, 1.2 °C higher than the former. The difference is because the traditional method gets the figure from the average of only three weather stations, while the satellite method obtains it from the average of thousands of DI pixels of the whole basin.

The efficiency of the satellite-estimated DI has benefited from the higher resolution LST image. Based on the sharpened 10m-resolution LST image (Fig. 7), air temperature and relative humidity can be retrieved in more spatial detail. As shown in the studies mentioned previously, the determination coefficients ( $R^2$ ) of regression equations for deriving air temperature using MODIS/AVHRR LSTs generally range from 0.54 to 0.79 [19] [32] [43], while it achieves to 0.82 in this study. This can be explained in following two reasons:

(1) The 100 m resolution of Landsat TIRS image is much higher than that of MODIS/AVHRR thermal images that are generally coarser than 1000 m. The sharpening of 100 m TIRS LST image to 10 m further enhances the accuracy of the TIRS LST because it greatly reduces the mixed pixel phenomenon. The results of Ma et al. [32] also show that a sharpened MODIS LST at 250 m resolution has a higher correlation with air temperature than the MODIS LST at 1000 m resolution. As indicated by Nichol [26], the sharpened LST can increase accuracy in the computation of temperature since it can improve the relationship between the LST image values and air temperature and enable the observation of micro-scale temperature patterns. Jones et al. [19] also pointed out that high resolution LST imagery could enhance the small scale temperature variations.

(2) There are errors occurring in the MODIS LST products. The validation of Wan et al. [44] indicated that MODIS LST products have an absolute bias of less than one degree Kelvin. Further validation carried out by Wang et al. [45] suggested an absolute bias of MODIS LST products ranging from 0.8 to 3°C. The inherent errors in the MODIS LST product would lower the agreement between in situ-measured and derived air temperatures.

## 5. Conclusions

The combination of air temperature and relative humidity has served to predict thermal comfort condition with DI measurements for decades. However, the traditional weather station-derived DI is incapable of revealing spatial details of thermal comfort in a city as its result is often represented only by a single DI value. By comparison, the satellite-based method can overcome this problem because it provides a DI image rather than a single value, which is composed of thousands of DI values showing spatial variations. This allows urban and building designers to have a better understanding of spatial differences in energy requirement for cooling in a city.

The visualization of DI spatial variability is achieved by combining remotely-sensed thermal infrared data with in situ-measured meteorological data. The DI map can be produced by using thermal infrared image derived air temperature and relative humidity. The DI map reveals spatial differences of human thermal discomfort sensation in a city and determines the differences in the characteristics of living environments among different DI levels. This adds new value to the traditional DI usage and expands the application range.

The proposed method provides a 10 m-resolution DI image that describes spatially-detailed DI patterns of the Fuzhou basin in summer of 2016. The DI image shows that though the hot weather makes people feel uncomfortable, the satellite-derived DI can still distinguish three different sensation levels ranging from Grades 4 to 6. The three DI grades clearly reflect the differences in living environments regarding to the percentages of building, vegetation and water covers.

Regression analysis shows that high building density significantly enhances human discomfort sensation, while vegetation and water helps to reduce the sensation. Nevertheless, the contribution of building density on DI is much higher than that of vegetation and water body. Its impact is nearly two times greater than the sum of the vegetation and water in the study case. Therefore, reducing building density is critical to decrease human discomfort sensation.

The method for producing satellite-estimated DI proposed in this study is useful for evaluating the spatial details of thermal comfort levels over a large area but not for forecast because the temporal resolution of the Landsat 8 satellite overpass at every 16 days is too low for weather forecast.

## Acknowledgements

This work was supported by the National Natural Science Foundation of China [grant number: 41501469, 2016] and Fujian Provincial Bureau of Surveying, Mapping and Geoinformation, China [grant number: 2017JX02]. Special thanks go to all the participants in the field measurements of the meteorological data.

## References

- [1] M. Georgescu, M. Moustauoui, A. Mahalov, J. Dudhia, Summer-time climate impacts of projected megapolitan expansion in Arizona, *Nature Climate Change* 3 (2013) 37–41.
- [2] K.W. Oleson, A. Monaghan, O. Wilhelmi, M. Barlage, N. Brunzell, J. Feddema, L. Hu, D.F. Steinhoff, Interactions between urbanization, heat stress, and climate change, *Climatic Change* 129 (2015) 525–541.
- [3] M.I. Stathopoulou, C. Cartalis, I. Keramitsoglou, M. Santamouris, Thermal remote sensing of Thom's discomfort index (DI): Comparison with in-situ measurements, *Proceedings of SPIE 5983, Remote Sensing for Environmental Monitoring, GIS Applications, and Geology* (2005) 5983–5990. <http://dx.doi.org/10.1117/12.627541>.
- [4] Y. Epstein, D.S. Moran, Thermal comfort and the heat stress indices, *Industrial Health* 44 (2006) 388–398.
- [5] G.V. Mostovoy, R.L. King, K.R. Reddy, V.G. Kakani, M.G. Filippova, Statistical estimation of daily maximum and minimum air temperatures from MODIS LST data over the state of Mississippi, *GIScience and Remote Sensing* 43 (2006) 78–110.
- [6] A. Benali, A.C. Carvalho, J.P. Nunes, N. Carvalhais, A. Santos, Estimating air surface temperature in Portugal using MODIS LST data, *Remote Sensing of Environment* 124 (2012) 108–121.
- [7] S. Carlucci, L. Pagliano, A review of indices for the long-term evaluation of the general thermal comfort conditions in buildings, *Energy and Buildings* 53 (2012) 194–205.
- [8] S. Carlucci, L. Pagliano, A. Sangalli, Statistical analysis of the ranking capability of long-term thermal discomfort indices and their adoption in optimization processes to support building design, *Building and Environment* 75 (2014) 114–131.
- [9] E.C. Thom, The Discomfort Index, *Weatherwise*, 12 (1959) 57–60.
- [10] P. J. Pennas, A Study on the discomfort index on the islands of Mediterranean Sea, *Archives for Metrology, Geophysics, and Bioclimatology, Ser. B*, 34 (1984) 365–373.
- [11] M.F.M. Din, Y.Y. Lee, M. Ponraj, D.R. Ossen, K. Iwao, S. Chelliapan, Thermal comfort of various building layouts with a proposed discomfort index range for tropical climate, *Journal of Thermal Biology*, 4 (2014) 16–15.
- [12] T.M. Giannaros, D. Melas, Study of the urban heat island in a coastal Mediterranean City: The case study of Thessaloniki, Greece, *Atmospheric Research* 118 (2012) 103–120.
- [13] W. Zhu, S. Zhang, Variation characteristics of comfort index of human body in China in recent 30 years, *Journal of Arid Meteorology* 30 (2012) 220–226.
- [14] M.S. Tselepidaki, C. Moustris, G. Pouloupoulou, Analysis of the summer discomfort index in Athens, Greece, for cooling purposes, *Energy and Buildings* 18 (1992) 51–56.
- [15] V. Silva, P. Azevedo, R.S. Brito, J. Campos, Evaluating the urban climate of a typically tropical city of northeastern Brazil, *Environmental Monitoring and Assessment* 161 (2010) 45–59.
- [16] J.N. Georgi, D. Dimitriou, The contribution of urban green spaces to the improvement of environment in cities: Case study of Chania, Greece, *Building and Environment* 45 (2010) 1401–1414.
- [17] D.K. Papanastasiou, D. Melas, H.D. Kambezidis, Air quality and thermal comfort levels under extreme hot weather, *Atmospheric Research* 152 (2015) 4–13.
- [18] A. Polydoros, C. Cartalis, Use of earth observation based indices for the monitoring of built-up area features and dynamics in support of urban energy studies, *Energy and Buildings* 98 (2015) 92–99.
- [19] P. Jones, Jr, G. Jedlovec, R. Suggs, S. Haines, Using MODIS LST to estimate minimum air temperatures at night, In: 13th Conference on Satellite Meteorology and Oceanography, American Meteorological Society,



- Norfolk, Virginia, (2004) 1–6.
- [20] H.Q. Xu, Analysis on urban heat island effect based on the dynamics of urban surface biophysical descriptors, *Acta Ecologica Sinica* 31 (2011) 3890–3901.
- [21] K. Pantavou, G. Theoharatos, A. Mavrakakis, M. Santamouris, Evaluating thermal comfort conditions and health responses during an extremely hot summer in Athens, *Building and Environment* 46 (2011) 339–344.
- [22] B.D. Giles, C. Balafoutis, P. Maheras, Too hot for comfort: the heat waves in Greece in 1987 and 1988, *International Journal of Biometeorology* 34 (1990) 98–104.
- [23] J.A. Barsi, J.R. Schott, S.J. Hook, N.G. Raqueno, B.L. Markham, R.G. Radocinski, Landsat-8 Thermal Infrared Sensor (TIRS) vicarious radiometric calibration, *Remote Sensing* 6 (2014) 11607–11626.
- [24] USGS. 2015. Landsat 8 Data. <http://landsat.usgs.gov>. (2016.8.12)
- [25] J.C. Jiménez-Muñoz, J.A. Sobrino, D. Skokovi'c, C. Mattar, J. Cristóbal. Land surface temperature retrieval methods from Landsat-8 Thermal Infrared Sensor data, *IEEE Geoscience and Remote Sensing Letters* 11 (2014) 1840–1843.
- [26] J. Nichol, An emissivity modulation method for spatial enhancement of thermal satellite images in urban heat island analysis, *Photogrammetric Engineering and Remote Sensing* 75 (2009) 547–556.
- [27] J.A. Barsi, J.R. Schott, F.D. Palluconi, S.J. Hook, Validation of a web-based atmospheric correction tool for single thermal band instruments, *Earth Observing Systems X, Proceedings of SPIE* 5882 (2005), San Diego, CA. doi: 10.1117/12.619990
- [28] G. Rigo, E. Parlow, D. Oesch, Validation of satellite observed thermal emission with in-situ measurements over an urban surface, *Remote Sensing of Environment* 104 (2006) 201–210.
- [29] N. Agam, W.P. Kustas, M.C. Anderson, F. Li, C.M.U. Neale, A vegetation index based technique for spatial sharpening of thermal imagery, *Remote Sensing of Environment* 107 (2007) 545–558.
- [30] J.W. Rouse, R.H. Haas, Jr., J.A. Schell, D.W. Deering, Monitoring vegetation systems in the Great Plains with ERTS. *Proceedings of the Third ERTS Symposium, NASA SP-351*. Washington DC, USA, 1 (1973) 309–317.
- [31] C. Vancutsem, P. Ceccato, T. Dinku, S.J. Connor, Evaluation of MODIS land surface temperature data to estimate air temperature in different ecosystems over Africa, *Remote Sensing of Environment* 114 (2010) 449–465.
- [32] W. Ma, L. Zhou, H. Zhang, Y. Zhang, X. Dai, Air temperature field distribution estimations over a Chinese mega-city using MODIS land surface temperature data: The case of Shanghai, *Frontier Earth Science* 10 (2016) 38–48. DOI 10.1007/s11707-015-0510-y.
- [33] H. Xu, A new index for delineating built-up land features in satellite imagery, *International Journal of Remote Sensing* 29 (2008) 4269–4276.
- [34] H. Q. Xu, Modification of normalised difference water index (NDWI) to enhance open water features in remotely sensed imagery, *International Journal of Remote Sensing* 27 (2006) 3025–3033.
- [35] W. Essa, B. Verbeiren, J. van der Kwast, T. Van de Voorde, O. Batelaan, Evaluation of the DisTrad thermal sharpening methodology for urban areas, *International Journal of Applied Earth Observation and Geoinformation* 19 (2012) 163–172.
- [36] M.K. Ghosh, L. Kumar, C. Roy, Monitoring the coastline change of Hatiya Island in Bangladesh using remote sensing techniques, *ISPRS Journal of Photogrammetry & Remote Sensing* 101 (2015) 137–144.
- [37] A. Ogilvie, G. Belaud, C. Delenne, J. Bailly, J. Bader, A. Oleksiak, L. Ferry, D. Martin, Decadal monitoring of the Niger Inner Delta flood dynamics using MODIS optical data, *Journal of Hydrology* 523 (2015) 368–383.
- [38] D. Yamazaki, M.A. Trigg, D. Ikeshima, Development of a global ~90 m water body map using multi-temporal

- Landsat images, *Remote Sensing of Environment* 171 (2015) 337–351.
- [39] S.J. Goetz, , R.K. Wright, A.J. Smith, E. Zinecker, E. Schaub, IKONOS imagery for resource management: Tree cover, impervious surfaces, and riparian buffer analyses in the mid-Atlantic region, *Remote Sensing of Environment* 88(2003) 195–208.
  - [40] J.R. Jensen, *Introductory Digital Image Processing: A Remote Sensing Perspective*, fourth ed., Pearson Prentice-Hall Inc, New Jersey, 2015.
  - [41] A. Onishi, X. Cao, T. Ito, F. Shi, H. Imur, Evaluating the potential for urban heat-island mitigation by greening parking lots, *Urban Forestry & Urban Greening* 9 (2010) 323–332.
  - [42] J.S. Wilson, M. Clay, E. Martin, D. Stuckey, K. Vedder-Risch, Evaluating environmental influences of zoning in urban ecosystems with remote sensing, *Remote Sensing of Environment*, 86 (2003) 303–321.
  - [43] G. Fu, Z. Shen, X. Zhang, P. Shi, Y. Zhang, J. Wu, Estimating air temperature of an alpine meadow on the northern Tibetan Plateau using MODIS land surface temperature, *Acta Ecologica Sinica* 31 (2011) 8–13.
  - [44] Z. Wan, Z.L. Li, A physics-based algorithm for retrieving land-surface emissivity and temperature from EOS/MODIS data, *IEEE Transactions on Geoscience and Remote Sensing* 35 (1997) 980–996.
  - [45] W.H. Wang, S.L. Liang, T. Meyers, Validating MODIS land surface temperature products using long-term nighttime ground measurements, *Remote Sensing of Environment* 112 (2008) 623–635.

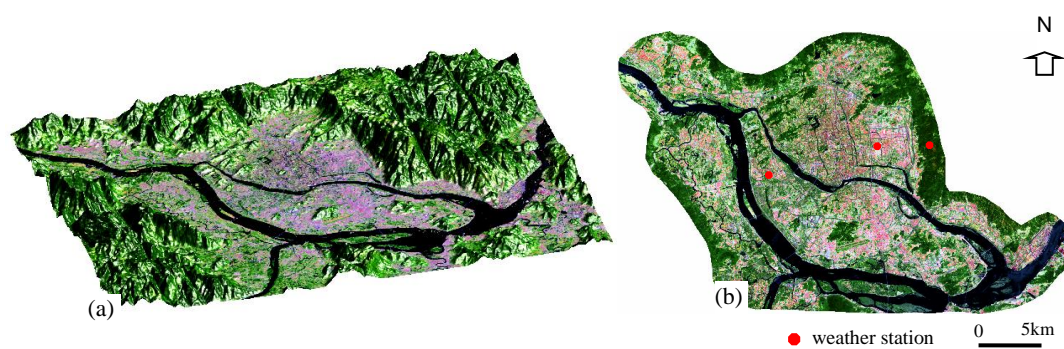


Fig. 1 Landsat 8 image of the Fuzhou basin (a) and the study area (b) (color should be used online only)

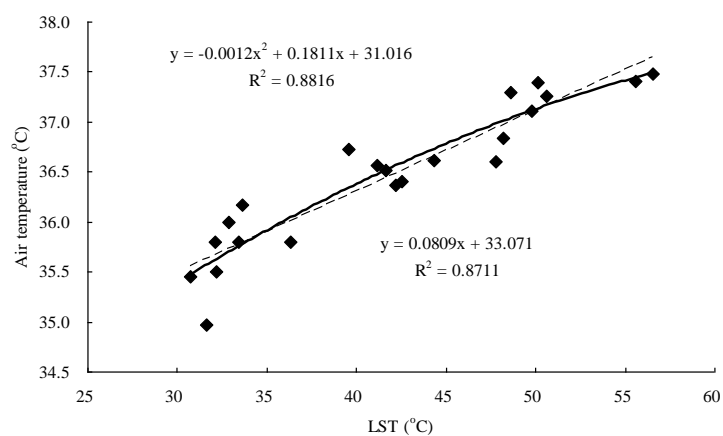


Fig. 2 Regression analysis between air temperature and LST (Solid line: polynomial, Dash line: linear)

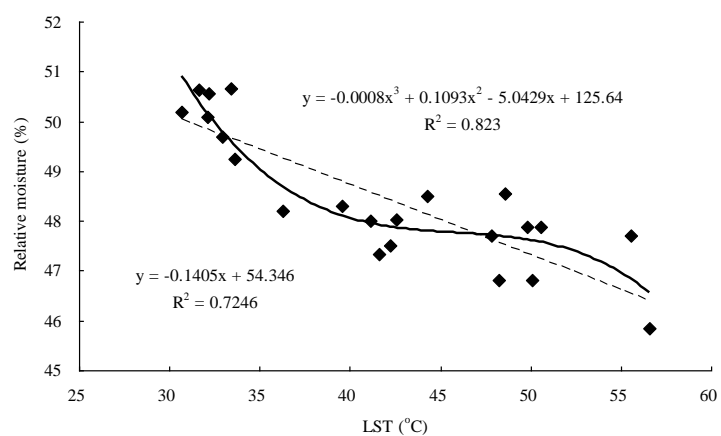


Fig. 3. Regression analysis between relative humidity and LST (Solid line: polynomial, Dash line: linear)

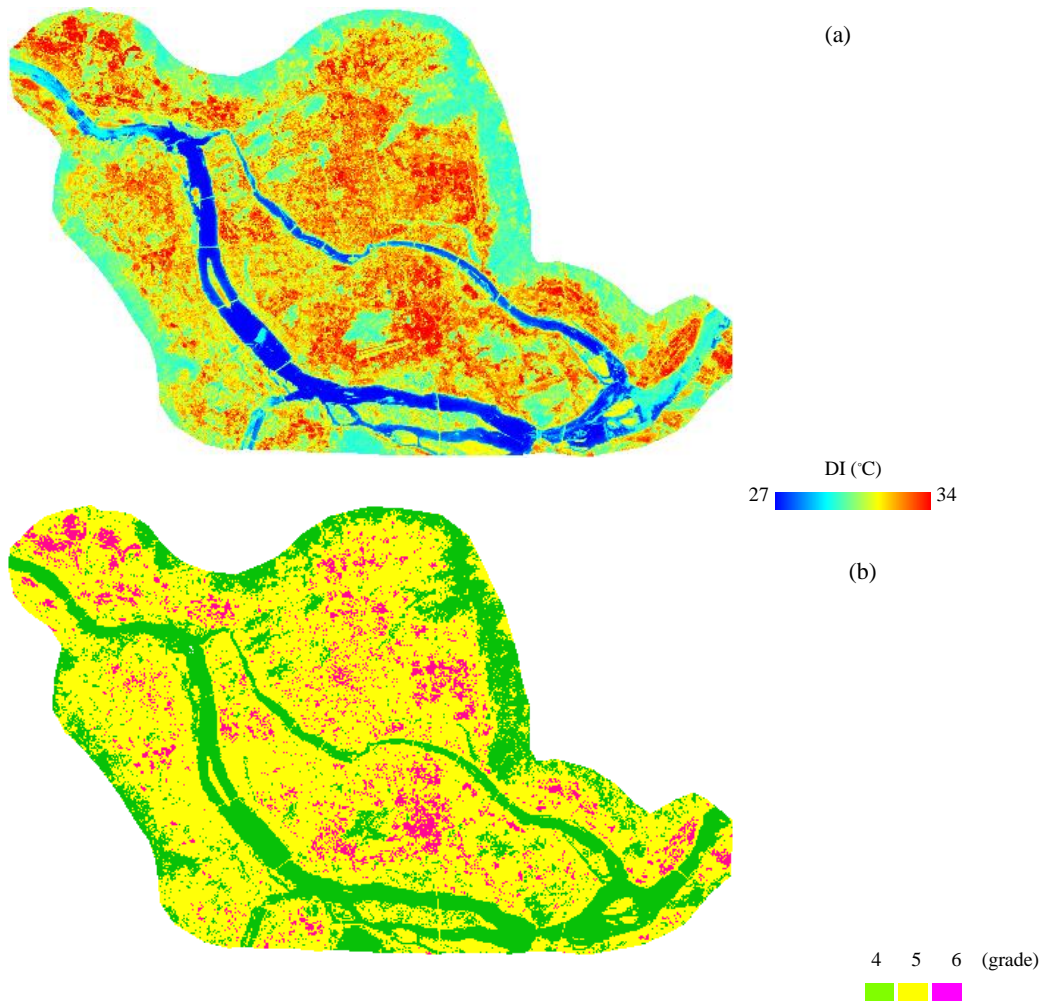


Fig. 4 The DI image of the Fuzhou basin (a) and its 3-grade map (b) (color should be used online only)



Fig. 5 Representative sub-images showing typical human living environment of each DI grade (a: Grade 4, b: Grade 5, c: Grade 6) (color should be used online only)

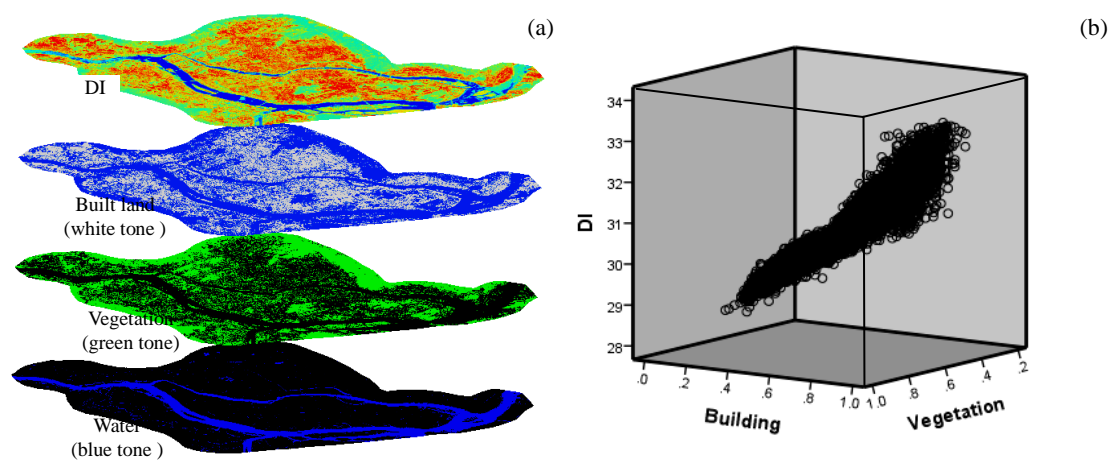


Fig. 6. DI, built land, vegetation, and water images (a) and a 3-D scatter plot showing the relationship among the first three images (b) (color should be used online only)



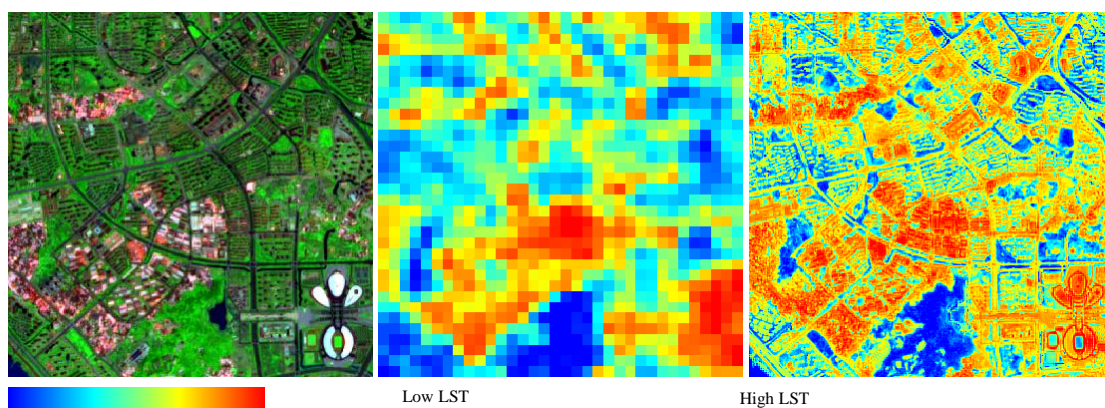


Fig. 7. Sentinel 2A-assisted sharpening of a TIRS 100m-resolution LST image to a 10m-resolution LST image. (Left: Sentinel 2A image, Middle: TIRS 100m LST image, Right: sharpened 10m LST image) (color should be used online only)

Table 1 Meteorological data of Fuzhou Wushan National Datum Weather Station (Station No. 58847)

Date	Local time	Sea level pressure (hPa)	Air temperature (°C)	Relative humidity (%)	Precipitation (mm)
06-23-2016	11: 00	1007.8	33.7	61	0
06-24-2016	11: 00	1007.1	33.6	61	0
06-25-2016	11: 00	1007.9	34.0	58	0

Source: China Meteorological Data Network (<http://data.cma.cn/data> )

Table 2 Average air temperature and relative humidity of measured objects on June 24, 2016

Surface object	Air temperature (°C)	Relative humidity (%)
Dark stone slab (1)*	36.60	47.70
Dark stone slab (2)	36.84	46.80
Dark stone slab (3)	37.40	46.80
Light stone slab (1)	36.40	48.03
Light stone slab (2)	36.57	48.00
Light stone slab (3)	36.51	47.34
Pervious brick (1)	36.62	48.50
Brick (1)	37.30	48.55
Asphalt road (1)	37.40	47.71
Asphalt road (2)	37.48	45.85
Cement roof (1)	37.11	47.87
Cement roof (3)	37.26	47.84
Bare soil (1)	36.37	47.50
Grass (1)	36.73	48.30
Grass (2)	35.80	48.20
Shrub (1)	36.17	49.25
Shrub (2)	36.00	49.70
Shrub (3)	35.45	50.20
Tree (1)	35.80	50.65
Tree (2)	35.50	50.55
Water (1)	34.98	50.63
Water (2)	35.80	50.10

\* The number within the bracket represents the serial number of three measurement sites

Table 3 Comparison of in situ meteorological data and satellite-estimated data of June 25, 2016

Weather station	Weather station data			Satellite-estimated data			Difference			Percent difference		
	AT	RH	<b>DI</b>	AT	RH	<b>DI</b>	AT	RH	<b>DI</b>	AT	RH	<b>DI</b>
	(°C)	(%)	(°C)	(°C)	(%)	(°C)	(°C)	(%)	(°C)	(%)	(%)	(%)
Wushan	33.42	60.81	<b>29.34</b>	33.96	62.96	<b>30.00</b>	0.54	2.15	<b>0.66</b>	1.62	3.54	<b>2.25</b>
Jin'an	34.17	58.38	<b>29.67</b>	35.36	58.90	<b>30.64</b>	1.19	0.52	<b>0.97</b>	3.48	0.89	<b>3.27</b>
FZU	33.49	58.96	<b>29.20</b>	33.99	61.76	<b>29.89</b>	0.50	2.80	<b>0.69</b>	1.49	4.75	<b>2.36</b>

AT: air temperature, RH: relative humidity

Table 4 Statistics of the 3-grade DI map and the characteristics of living environment of each grade

Grade	DI range (°C)	Area (km <sup>2</sup> )	Percentage (%)	Discomfort condition	Built cover (%)	Vegetation cover (%)	Water cover (%)
4	$27 \leq \text{DI} < 29$	155.31	26.63	Most of the population feels discomfort	1.02	50.48	48.50
5	$29 \leq \text{DI} < 32$	384.19	65.92	Everyone feels severe stress	55.07	38.05	3.88
6	$\text{DI} \geq 32$	43.44	7.45	State of medical emergency	96.51	3.30	0.19